

Theoretical and computational feasibility of femtosecond laser multifilament transverse structures reconstruction via circular-scanning-based photoacoustic tomography

Qingwei Zeng(曾庆伟), Lei Liu(刘磊), Shuai Hu(胡帅), and Shulei Li(李书磊)
Citation: Chin. Phys. B, 2025, 34 (**9**): 094209. DOI: 10.1088/1674-1056/ade663
http://cpb.iphy.ac.cn; http://iopscience.iop.org/cpb

What follows is a list of articles you may be interested in

Exciton dynamics and random lasing in surface-passivated CdSe/CdSeS core/crown nanoplatelets

Huan Liu(刘欢), Puning Wang(王谱宁), and Rui Chen(陈锐)
Chin. Phys. B, 2025, 34 (**9**): 094201. DOI: 10.1088/1674-1056/adcd46

Impact of free electron laser coherence on imaging quality

Shuang Wei(魏爽), Shuang Gong(龚爽), Yang Bu(步扬), and Zi-Jian Song(宋子健)
Chin. Phys. B, 2025, 34 (**5**): 054201. DOI: 10.1088/1674-1056/adb734

High peak power mini-array quantum cascade lasers operating in pulsed mode

Yuhang Zhang(章宇航), Yupei Wang(王渝沛), Xiaoyue Luo(罗晓玥), Chenhao Qian(钱晨灏), Yang Cheng(程洋), Wu Zhao(赵武), Fangyuan Sun(孙方圆), Jun Wang(王俊), and Zheng-Ming Sun(孙正明)
Chin. Phys. B, 2025, 34 (**1**): 014204. DOI: 10.1088/1674-1056/ad886b

Continuous wave and active *Q*-switched operation of Watt-level LED-pumped two-rod Nd,Ce:YAG laser

Jian-Ping Shen(沈建平), Peng Lu(芦鹏), Shao-Cong Xu(徐少聪), Rong-Rong Jiang(江容容), Yang Chen(陈阳), Liang Chen(陈亮), and Feng-Yang Xing(邢凤阳)
Chin. Phys. B, 2024, 33 (**7**): 074207. DOI: 10.1088/1674-1056/ad34c9

Elegant Ince–Gaussian breathers in strongly nonlocal nonlinear media

Bai Zhi-Yong(白志勇), Deng Dong-Mei(邓冬梅), and Guo Qi(郭旗)
Chin. Phys. B, 2012, 21 (**6**): 064218. DOI: 10.1088/1674-1056/21/6/064218

Theoretical and computational feasibility of femtosecond laser multifilament transverse structures reconstruction via circular-scanning-based photoacoustic tomography

Qingwei Zeng(曾庆伟)[1,2], Lei Liu(刘磊)[1,2,†], Shuai Hu(胡帅)[1,2,‡], and Shulei Li(李书磊)[1,2]

[1] *College of Meteorology and Oceanography, National University of Defense Technology, Changsha* 410073, *China*
[2] *Key Laboratory of High Impact Weather (Special), China Meteorological Administration, Changsha* 410074, *China*

(Received 30 December 2024; revised manuscript received 6 May 2025; accepted manuscript online 20 June 2025)

We theoretically investigate the feasibility of reconstructing the transverse structures of femtosecond laser filaments in air by photoacoustic tomography. To simulate the emission and transmission of filament-induced ultrasonic signals more truly, a series of experimentally recorded cross-sectional images are used to simulate the initial pressure rise from multiple filaments (MFs). The aperture size and sensitivity of the detector was incorporated into the reconstruction algorithm. The results show that frequency of acoustic signals induced by MFs with maximum volumetric energy density ~ 100 kJ/m^3 is about 2 MHz below. The initial spatial distribution of optical filaments can be clearly reconstructed with the back projection based algorithm. We recommend a PAT system with transducers of a lower central frequency and a stronger apodization working at a longer scanning radius can be used in photoacoustic image reconstruction of femtosecond laser multifilaments. This study demonstrates the feasibility of using photoacoustic tomography to reconstruct femtosecond multifilament images, which is helpful for studying the complex dynamic processes of multifilament and multifilament manipulation and is also valuable for the remote applications of laser filaments.

Keywords: femtosecond laser filaments, transverse structures, energy deposition, photoacoustic tomography, ultrasonic transducer, back projection

PACS: 42.55.–f, 42.65.–k, 44.05.+e, 43.60.+d

DOI: 10.1088/1674-1056/ade663 **CSTR:** 32038.14.CPB.ade663

1. Introduction

Laser filamentation is a dynamically self-guided propagation regime for ultrashort laser pulses caused by the combined action of the optical Kerr effect, and defocusing effects such as diffraction and plasma defocusing.[1] It has been observed experimentally that a plasma filament can persist for hundreds of meters and up to several kilometers in the ambient atmosphere without external focusing elements.[2] Over the years, this phenomenon in atmosphere or other gas media has been an active research area not only for its fundamental aspects of complex nonlinear physical effects but also for its very promising broad spectrum of applications, such as remote sensing,[3] weather modulating,[4] microwave guiding,[5] guiding of lightning,[6] and fog clearing.[7]

A stable and controllable femtosecond filament is a prerequisite for the above applications. However, due to the air refractive index disturbance caused by atmospheric turbulence and the random non-uniform distribution of laser pulse energy, the splitting of the optical filament is often prone to occur, which is the so-called multiple filaments. The formation of multiple filaments will limit the propagation distance of the optical filament, and also reduce the spot quality of the beam, thereby limiting the application of the optical filament in the actual atmosphere. Therefore, the study of position arrangement, quantity change and energy exchange mechanism during multifilament transmission has become a key issue in the research of optical filament manipulation, which also brings an imperative demand for diagnosing the spatiotemporal dynamics of filamentation.[8]

Many scholars have recognized that the acquisition of transverse cross-sectional distribution of optical filaments is beneficial to the visualization of dynamic processes of filaments. However, it is a challenge to directly detect the cross section of optical filament due to the extremely high intensity inside the optical filament, since almost any material inserted into a high-intensity laser beam will be destroyed.[9] The cross-sectional intensity patterns at different longitudinal positions along filament are mainly acquired by inserting any traditional detector in the channels.[9–11] However, this method will cause damage to the optical filament transmission. So far, several indirect methods such as plasma fluorescence,[12] terahertz radiation,[13] optical interferometry,[14] secondary electrical discharges,[15] and sonographic probing[16] have been developed to diagnose peculiarities of the plasma. Among

†Corresponding author. E-mail: liulei17c@nudt.edu.cn
‡Corresponding author. E-mail: hushuai2012@hotmail.com

© 2025 Chinese Physical Society and IOP Publishing Ltd. All rights, including for text and data mining, AI training, and similar technologies, are reserved.

those methods, the acoustic diagnosis based on observable photoacoustic effects demonstrates tremendous potential in measuring long-distance filamentation, with its advantages of fast, non-contact and high precision.[17,18] Since the amplitude of the acoustic signal is closely related to the intensity of the filamentation and the density of free electrons, the filamentation characteristics, such as onset, length, electron density, and relative intensity, can be rapidly evaluated by moving the kilohertz-range microphone sensor along the direction of filament propagation. The microphone array was also built to capture the dynamic full propagation path of femtosecond laser pulses in turbulent environments.[19] However, sonographic probing with a kilohertz-range microphone can only obtain the laser pulse's axial characteristics and its spatial resolution was too low to reveal any data on the spatial parameters of this channel, which limits the study of the dynamic energy exchange mechanism between optical filament core and the energy reservoir.[20,21]

In this article, an emerging medical imaging technique called photoacoustic tomography (PAT) has been introduced into the diagnosis of optical filament. The feasibility of using photoacoustic tomography to reconstruct the cross section of optical filament is verified theoretically. In contrast to previous reconstruction of single filament, we focus on the reverse reconstruction of more complex multifilaments. To the best of our knowledge, no one has done this before. To better assess the feasibility of the PAT method, a series of experimentally recorded cross-section images of multifilaments is used to initiate the ultrasonic propagation simulation. We also investigate the influence of finite aperture size and finite bandwidth on the reconstruction of cross-section images of filaments. We hope the research of this paper can provide useful guidance for diagnosis of filaments' spatial characteristics and multifilament modulation.

2. Simulation methods

The basic process of photoacoustic tomography involves excitation of acoustic pressure waves by illuminating an absorbing medium (e.g., biological tissue) with powerful pulsed lasers first, and one or more ultrasonic transducers are placed at a certain distance to collect acoustic signals. The acoustic signals recorded by the transducer are later used to map initial pressure rise or to reconstruct an image of the photoacoustic (PA) source distribution with an image reconstruction algorithm.[22] Here, we first describe the forward simulation model and backward reconstruction algorithm in detail.

2.1. Forward photoacoustic signal simulation

The forward problem involves finding pressure signals at a specific distance and time. Basically, the physical mechanism behind sound generation from filamentation involves the sudden deposition of pulse energy in the propagation medium, which impulsively drives an outward-propagating cylindrical pressure and density wave that progressively transform into acoustic waves.[23] Essentially, a plasma filament mainly deposits energy into the propagation medium through optical field ionization and non-resonant rotational Raman excitation of the air molecules.[14] This implies that the time scales of the physical processes involved in the formation of acoustic signals induced by femtosecond laser filaments vary greatly, from the duration of the laser pulse ($\sim$ in unit fs) to the generation of strong shock waves ($\sim$ in unit μs). Therefore, it is very difficult to simulate the process completely. Here, we mainly focus on the basic physical processes. The gas dynamics after deposition of energy by an ultrashort optical pulse has mainly been considered in the forward simulation. According to the transmission characteristics of the optical filament, PAT with a circular scanning or spherical scanning geometry is considered to record the filament-induced acoustic signals. A schematic diagram of a typical PAT scanning geometry is shown in Fig. 1(a). In practice, several ultrasound transducers (detectors) are placed at various angular positions on the circumference of the circle to record the PA signals coming from the filaments. For simplicity, we have performed all simulations and reconstructions in two dimensions without loss of generality. For transducers at the specified position $\boldsymbol{r}$, the received sound pressure signal is described by the following photoacoustic wave equation in an acoustically lossless fluid medium:[24]

$$\frac{\partial \boldsymbol{u}}{\partial t} = -\frac{1}{\rho_0}\nabla p, \tag{1}$$

$$\frac{\partial \rho}{\partial t} = -\rho_0 \nabla \cdot \boldsymbol{u} - \boldsymbol{u} \cdot \nabla \rho_0, \tag{2}$$

$$p = c_0^2 \left(\rho + \boldsymbol{d} \cdot \nabla \rho_0 - L\rho\right), \tag{3}$$

where $\boldsymbol{u}$ is the acoustic particle velocity, p is the acoustic pressure, ρ is the acoustic density, ρ_0 is the ambient density (it stands for air here), and $c_0 = 330$ m/s is the isentropic sound speed. L is the loss operator, which is defined as

$$L = \tau \frac{\partial}{\partial t}\left(-\nabla^2\right)^{\gamma/2-1} + \eta\left(-\nabla^2\right)^{(\gamma+1)/2-1}. \tag{4}$$

Here τ and η are absorption and dispersion proportionality coefficients, respectively, which can be defined by

$$\tau = -2\alpha_0 c_0^{\gamma-1}, \quad \eta = 2\alpha_0 c_0^{\gamma} \tan\left(\pi\gamma/2\right), \tag{5}$$

where α_0 is the power law prefactor in Np (rad/s)$^{-\gamma}$·m^{-1} and γ is the power law exponent.

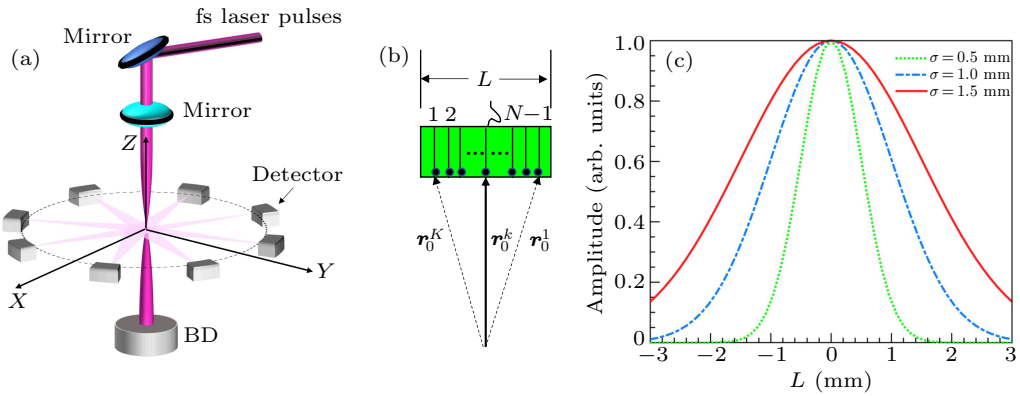


Fig. 1. Schematic diagram of (a) the measurement system for filament-induced acoustic signals, (b) the division of detection points on the surface of the transducer, and (c) apodization conditions of transducer with axisymmetric Gaussian form.

The detection surface of an ultrasonic transducer used in the practical photoacoustic tomography measurement system is usually flat and can reach a few millimeters in size. This is because such transducers are readily available on the market and provide a good signal-to-noise ratio. Moreover, the detectors actually used are mostly bandwidth-limited ultrasound transducers. The spatial resolutions of measurement has been verified to depend on the finite bandwidth of the ultrasound detection system and the size of the transducer aperture.[25] Therefore, both two factors need to be considered in the forward simulation. Here, we divided the recording surface of the transducer into many point detectors rather than a circular surface, as shown in Fig. 1(b).

In addition, in most studies, the sensitivity of the detector surface is assumed to be constant throughout the aperture, which is not consistent with the actual characteristics of the transducer. Thus, a gaussian apodization function was used to describe the sensitivity of transducer surface[25]

$$W\left(\boldsymbol{r}_0^i\right) = \exp\left(-\frac{\left|\boldsymbol{r}_0^i - \boldsymbol{r}_0^k\right|^2}{2\sigma^2}\right), \tag{6}$$

where σ is the standard deviation of the Gaussian apodization function, $\boldsymbol{r}_0^k$ is the k-th point detector, and $\boldsymbol{r}_0^i$ is the receiving position of the i-th transducer. The contribution from different elements of the detector surface to the total signal of the detector is shown in Fig. 1(c). The central part of the sensor is the most sensitive, and areas away from the center are less sensitive. The pressure signal recorded at position $\boldsymbol{r}_0$ can be expressed as a surface integral over the detector aperture[26]

$$p'\left(\boldsymbol{r}_0, t\right) = \iint p\left(\boldsymbol{r}'_0, t\right) W\left(\boldsymbol{r}_0^i\right) \mathrm{d}^2 \boldsymbol{r}_0^i. \tag{7}$$

2.2. Reconstruction algorithms

In PAT, we essentially deal with an inverse problem. The inverse problem of photoacoustic tomography is to reconstruct the initial pressure rise or deposited energy from the measured (recorded) acoustic signals. To date, various reconstruction algorithms have been developed to map the initial pressure rise distribution inside the absorber, including analytical algorithms and model-based iterative image reconstruction algorithms. The back-projection method is the most widely used image reconstruction techniques due to its simplicity, robustness and computational efficiency.[27] Xu *et al.*[28] deduced a universal back-projection formulas for planar and cylindrical geometry. However, the formula is in the Fourier domain and involves multiple integrals or series summations, which makes it complicated to implement. Therefore, a simplified time domain reconstruction formula known as the universal back-projection algorithm (UBP) is more used, which calculates the initial pressure rise in the time domain by means of backprojection as follows:[29]

$$p_0\left(\boldsymbol{r}\right) = \int_{\Omega_0} b\left(\boldsymbol{r}_0, t = \frac{\left|\boldsymbol{r} - \boldsymbol{r}_0\right|}{c}\right) \frac{\mathrm{d}\Omega_0}{\Omega}, \tag{8}$$

$$b\left(\boldsymbol{r}_0, t\right) = 2p\left(\boldsymbol{r}_0, t\right) - 2ct\frac{\partial p\left(\boldsymbol{r}_0, t\right)}{\partial t}, \tag{9}$$

$$\mathrm{d}\Omega_0 = \frac{\mathrm{d}S_0}{\left|\boldsymbol{r} - \boldsymbol{r}_0\right|^2}\left[\boldsymbol{n}_0 \cdot \frac{\left(\boldsymbol{r} - \boldsymbol{r}_0\right)}{\left|\boldsymbol{r} - \boldsymbol{r}_0\right|}\right], \tag{10}$$

where Ω_0 is the solid angle subtended by the entire measurement surface. S_0 with respect to the reconstruction point $\boldsymbol{r}$ inside S_0. $\mathrm{d}\Omega_0$ is the solid angle subtended by detection element $\mathrm{d}S_0$ with respect to reconstruction point at $\boldsymbol{r}$. The term $\mathrm{d}\Omega_0/\Omega_0$ is a factor weighing the contribution to the reconstruction from the detection element $\mathrm{d}S_0$. $b\left(\boldsymbol{r}_0, t\right)$ is the back-projection term. Pramani[26] developed a simple delay-and-sum algorithm to implement this backprojection formula. In this paper, the delay-and-sum (DAS) algorithm is also used to reconstruct transverse image of multifilaments, which suit well for PAT system with circular scanning geometry.[30] To overcome the image quality reduction associated with the well-known "finite aperture effect", the shape and aperture size of the transducer must be considered in the reconstruction algorithm.[27] Therefore, both the conventional delay-and-sum (CDAS) algorithm and the modified delay-and-sum (MDAS) algorithm are employed to reconstruct the cross-sectional images of MFs. The difference between these two methods

mainly lies in how to process the acoustic signal on the surface of the transducer.[14] As for conventional delay-and-sum reconstruction, the large-aperture detector is treated as a point located at the center of the detector. The PA signals recorded by point detectors at the surface of a flat piezoelectric transducer are spatially averaged first and then are backprojected from the central point of the transducer surface to form an image. In the modified delay-and-sum reconstruction algorithm, the entire area of the transducer (in this case a line) is considered. The line transducer was divided into many small segments and acoustic signal from each receiving point is back projected to the imaging area instead of one single point at the center of the transducer. Then the same process is repeated for other transducer positions as well. Refer to Fig. 1 of Ref. [25] for more details.

3. Results and discussion

3.1. Characteristics of multifilaments induced acoustic signals

Theoretically, by solving the forward problem, the PA pressure at a field point can be estimated if the spatial distribution of the initial pressure rises in the plasma region is known. Thus, the open-source acoustics toolbox *k*-wave is used to numerically resolved the above forward model in time-domain.[31] The *k*-space pseudospectral method is used in the toolbox to effectively reduce the memory and number of steps required for accurate simulations. For simplicity, we performed all simulations and reconstructions in two dimensions without loss of generality. To perform photoacoustic simulation, the spatial profile of initial pressure rise from multifilaments needs to be known first. The formation of pressure pulse is closely related to local nonstationary medium heating, which take place at a ns timescale.[32] Thus, the relationship between the initial pressure distribution and the heat source can be approximated as $p_0(\boldsymbol{r}) = \beta c_0^2 Q(\boldsymbol{r})/C_v$, where $Q(\boldsymbol{r})$ is the absorbed energy density distribution, β is volumetric thermal expansion coefficient, and C_v is specific heat capacity at constant volume. In the existing literature, in order to simplify the numerical solution of the forward equations, the initial pressure distribution is often assumed to be of Gaussian form.[20] This simplification is reasonable for the study of single filament, but not suitable for the study of multi-filaments with complex structures. In this paper, the initial pressure rise from laser filaments is simulated by a series of experimentally recorded multifilament cross-section images as shown in Fig. 2. These figures characterize propagation of Teramobile laser beam (220 mJ, 600 fs) in cloudy atmosphere, which are quoted from Ref. [33]. We processed the pictures as follows: firstly, after loading the picture in Matlab, we get its gray value; Secondly, when the gray value of a pixel in the picture is less than the specified value, the gray value of the corresponding pixel is set to 0. Other gray values greater than the specified value remain unchanged. That is, outside the targets there is no initial pressure rise. Finally, a moving average filter function is used to smooth the image. Figure 2(a) shows the spatial distribution of the smoothed multifilament cross section. As shown in the processed image, such treatment can clearly show a structure of a high intensity "core" region and a surrounding photon bath as revealed by some experimental measurements.[34]

Planar transducers with 3-mm active area diameter were employed to record the time-dependent pressure signal at distances of 5 mm from scanning center. The whole circular scanning system consists of 64 planar transducers arranged uniformly. We have used a 1.0-MHz center frequency with 70% nominal bandwidth detectors. During the simulation, surface of a transducer is divided into 51 line segments as set in Ref. [26]. To simulate the signal received by the large detector, the pressure waves at several grid points (falling on the detector surface, in our case the detector line) are recorded. For the convenience of post-processing, 51 time-dependent pressure fields are stored in a file as signals received by the same transducer. The sample interval was 10 ns, and the PA pressure values at 6048 time points were saved for each point detector. The corresponding image domain is 12 mm in both x and y directions. The computational grid of 2064×2064 pixels with a perfectly matched boundary layer (2 mm in width) was used for the generation of acoustic pressure waves at the grid points in *k*-wave. The imaging region is restricted to 1024×1024 grid points with a square of size 4 mm×4 mm, which is placed at the center of the computational domain. In all the simulations, the sound speed in the air is assumed to be 330 m/s. In order to consider the attenuation of the acoustic signal in the air, an exponential decay relationship with power law prefactor $\alpha = 0.185$ [in units of dB/(MHz^2·cm)] and power law exponent $\gamma = 2.0$ (dimensionless parameter) is used.[35] All the simulations and reconstructions were executed on a personal workstation with two i7 Intel 64-bit processors and a total of 64-GB RAM.

The time profiles and amplitude of acoustic waves induced by filaments are mainly determined by the energy of the laser pulse and its focusing conditions.[35] Therefore, we first studied the characteristics of acoustic signal induced by optical filaments with different volumetric energy density. The absorbed energy density distribution is assumed to be $Q(\boldsymbol{r}) = H_0 \times H(\boldsymbol{r})$, where H_0 is the maximum volumetric energy density and $H(\boldsymbol{r})$ is the normalized initial intensity distribution of MFs as shown in Fig. 2(a). During the simulation, the maximum volumetric energy density H_0 is set to be 10 kJ/m^3, 50 kJ/m^3,100 kJ/m^3, and 300 kJ/m^3, which is consistent with typical plasma density of $\sim 2 \times 10^{16}$ cm^{-3} and rotational heat-

ing of 4 meV/molecule.[20] As shown in Fig. 2(b), the intensity of sound pressure increases with the increase of maximum volumetric energy density. The pressure signal generated by multifilaments has the typical characteristic of piezoelectric signal, corresponding to a steep positive pressure peak followed by a negative pressure region.[36] Unlike the clear *N*-shape structure of single filament, the multifilaments induced pressure pulse exhibit a distinct multiple peaks structure in the positive pressure peak, which happens to be associated with multifilament hotspots at different distances from the transducer. The amplitude and pulse duration of the acoustic signal increases with the increase of the maximum volumetric energy density H_0. The typical acoustic pulse duration is roughly 20 μs, which is consistent with the measurement results of microphone.[37] The frequency features of the acoustic emission provide relevant information on the conversion of laser energy to acoustic energy.[8] As can be seen from Fig. 2(c), the frequency spectra of the pressure generated by multifilaments with different volumetric energy density H_0 are mostly below 2 MHz when propagated up to 5 mm away from the center through attenuation. The acoustic spectrum range is of a similar magnitude to the experimental measurements.[38] The spectral bandwidth of the acoustic pulse emitted from the optical filament is considered as an indicator of the filament intensity distribution, which is positively correlated with the laser filament intensity.[8] Uryupina[20] found the maximum of the spectrum of theoretical acoustic signal from a single filament is at the frequency of 1.16 MHz. The value seems to be larger than our results, which may relate to their closer recording distance (4 mm). The maximum acoustic bandwidth of acoustic signal induced by a femtosecond laser pulse at a given laser energy is experimentally found to increases from 0.7 MHz to 1.65 MHz as the focal lengths increase from 5 cm to 5 m,[37] which is consistent with our simulation results and also indirectly illustrate the reliability of our simulation model. In short, a transducer operating in the megahertz frequency is theoretically sufficient for the measurement of filaments' acoustic signals. Moreover, from the comparison of three multifilament simulation results, it is obvious that the number and arrangement of optical filaments have an effect on the change of sound pressure signal and spectrum. The number of multiple peaks increases with the number and arrangement of optical filaments. The difference of the sound pressure signal or spectrum includes the information of the spatial structure of the optical filament, and also provides the possibility to reconstruct distribution image of the optical filament.[39]

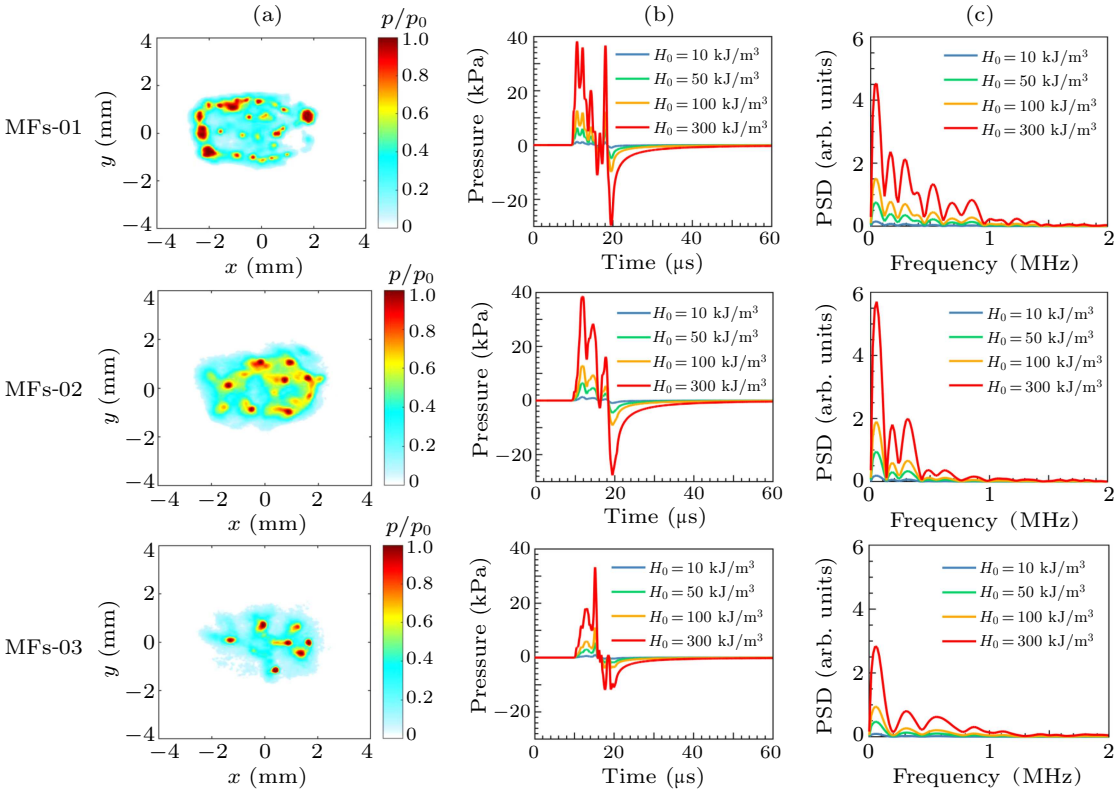


Fig. 2. The initial cross-section distribution conditions of multiple filaments (MFs). (a) The three smoothed initial intensity distributions of MFs (hereafter referred to as MFs-01, MFs-02, and MFs-03), (b) the simulated acoustic signals, and (c) the frequency spectrum for MFs different maximum volumetric energy densities at a distance of 5 mm from scanning center.

3.2. Influences of PAT reconstruction algorithms

The reconstructed images of three types of multifilament cross sections using CDAS and MDAS algorithms for a flat sensor are shown in Fig. 3. The reconstructed PAT images from conventional delay-and-sum (CDAS) algorithm with an ideal point detector (BPAD for short) are also presented in the

first column of Fig. 3. A 40-dB noise level was added. The width of the Gaussian function σ is set to 1.0 mm.

As shown in the first column of Fig. 3, the cross-sectional image of multiple filaments is well reconstructed by BPAD method with the ideal point detectors and there is no tangential blur, which is considered as a standard for subsequent comparisons. The second and third columns of Fig. 3 show the reconstructed images with a 3-mm active area transducer with traditional reconstruction and with modified reconstruction, respectively. The size of the core and the energy reservoir (the halo around the core) is basically distinguishable from the reconstructed pressure distribution. The negative visible blue areas around filament core are believed to relate to the filtering of low frequency components of the acoustic signals as all the detectors considered here are band limited.[36] There are some differences in the structure of the reconstructed images using the two methods. For CDAS algorithm, we find there is an elongation of the outside filaments in the tangential direction as indicated by red dotted box in Fig. 3(a), blue dotted box in Fig. 3(b), and purple dotted box in Fig. 3(c). The farther away from the scanning center, the larger the elongation (or the poorer tangential resolution). The arched elongated artifacts are typical for back-projection algorithm due to the limited number of receivers.[35] Due to the attenuation of the high-frequency components of the pressure pulse in air, peak value of the reconstructed pressure is smaller than its initial value. As shown in the third column of reconstructed images, the elongation along the tangential direction has been reduced with modified reconstruction. The MDAS algorithm preserves the shape of "hot spots" in the filaments very close to the ideal reconstruction, albeit with more negative areas. In all, the modified reconstruction is able to delineate the structures better than with traditional reconstruction and it is well suited for the reconstruction of multifilament's cross section.

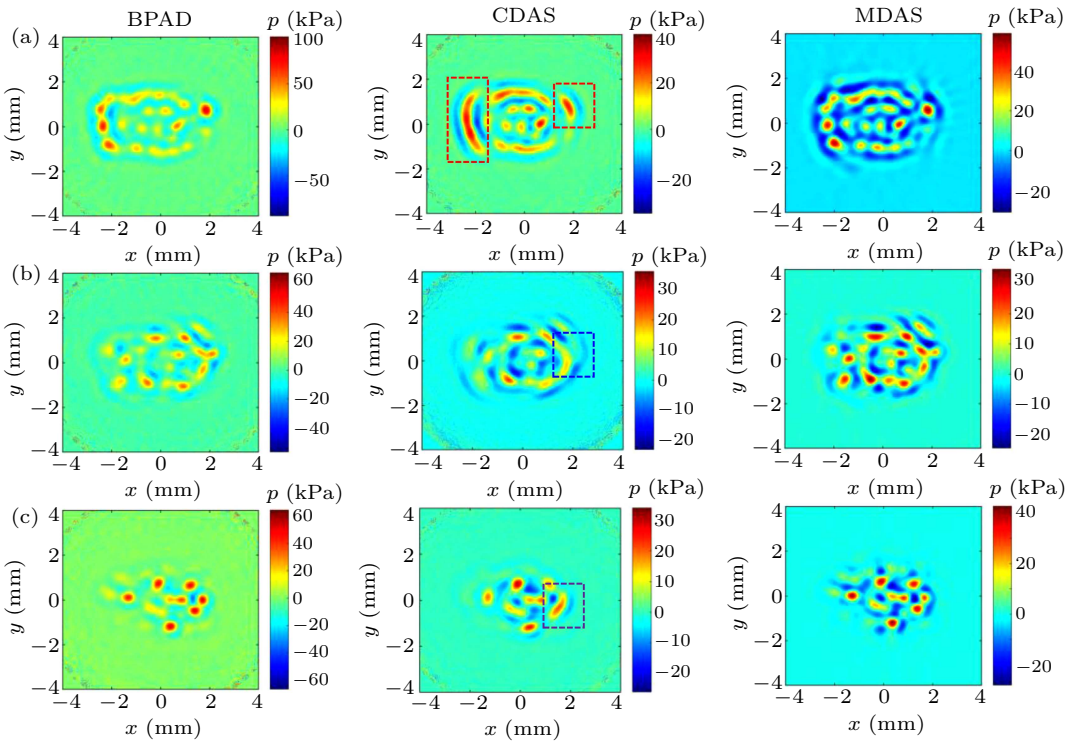


Fig. 3. The reconstructed images with different reconstruction algorithms for (a) MFs-01, (b) MFs-02, and (c) MFs-03.

3.3. Influences of PAT system parameters

In this section, PAT system parameters including central frequency f_c, aperture size L, and apodization condition of transducer σ are varied to examine their effect on image reconstruction. We also repeat the simulations for different scanning radius considered for data collection just to see if that has any effect on reconstruction results. For the convenience of expression, we only select MFs-01 for analysis. In fact, we have also analyzed the other two cases, but the conclusions are basically similar, so we will not analyze them too much here.

Figures 4(a) and 4(b) present the reconstructed images of MFs-01 from acoustic signals recorded by transducer with central frequency f_c based on CDAS algorithm and MDAS algorithm, respectively. It is shown that the tangential blur generally gets server as the central frequency gets higher for both algorithms. For CDAS algorithm, the filament, far from the center of the scan, is visibly elongated in a ring shape. The peak values of pressure in the filament hot spots decrease significantly with the increase of center frequency. Therefore, in photoacoustic tomography, transducers with appropriate center frequencies need to be selected according to the frequency range of the acoustic signal.

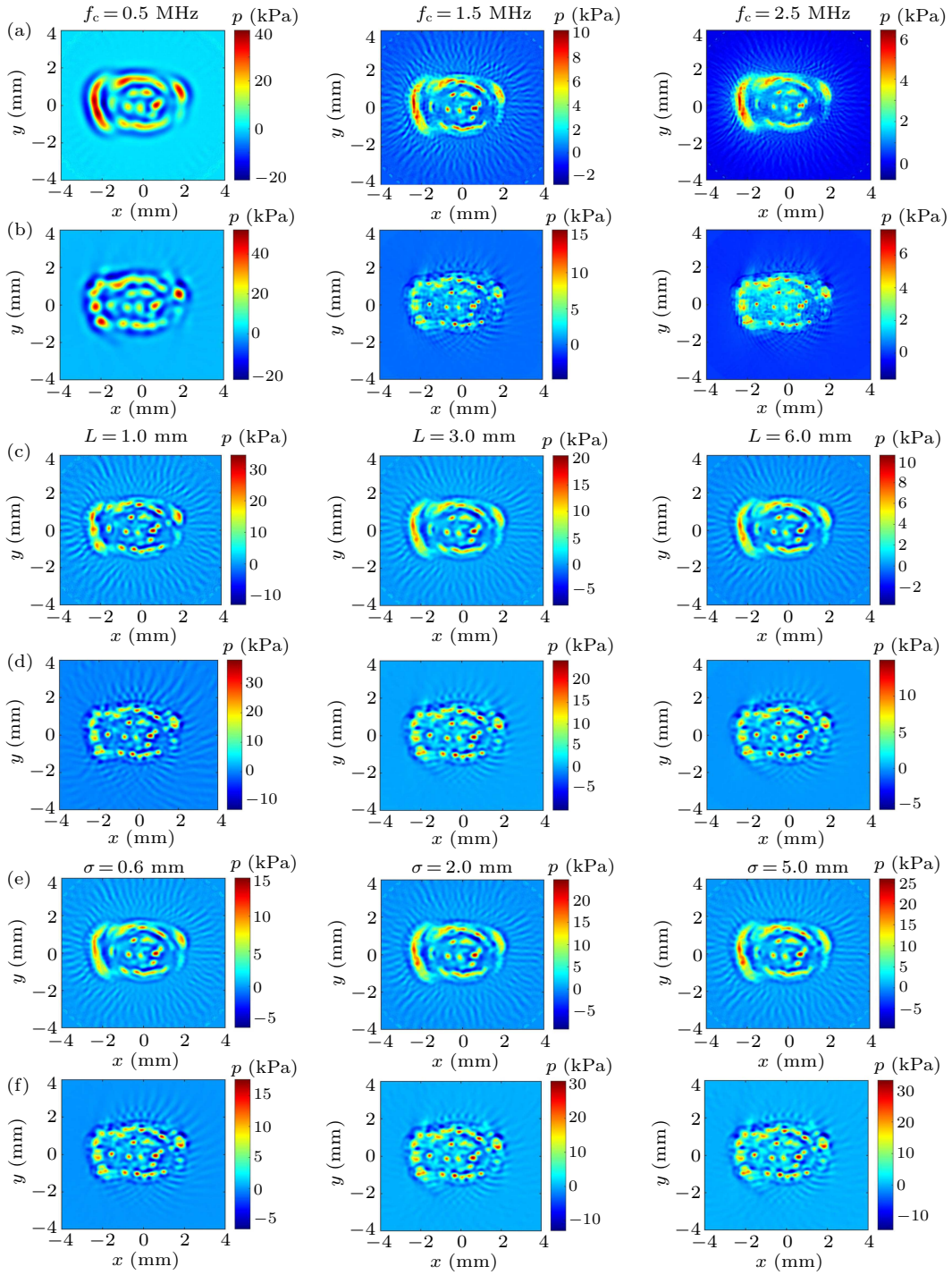


Fig. 4. Comparisons of reconstructed image with different [(a) and (b)] central frequency f_c, (c) and (d) apertures size L, and (e) and (f) apodization condition σ, where panels (a), (c), and (e) are images reconstructed by CDAS algorithm and panels (b), (d), and (f) are reconstructed by MDAS algorithm.

Figures 4(c) and 4(d) show the reconstructed images of MFs-01 with transducers of different aperture size L. For CDAS algorithm, the reconstructed image with $L = 1.0$ mm can reproduce the structural distribution of multifilaments well. However, the tangential resolution becomes worse as the aperture size of the transducer increases. This may be related to the fact that a smaller size of the transducer can accept signals from wider angles. However, the small-sized transducers have weaker sensitivity due to the high thermal noise.[25] Therefore, many researchers have tried to improve tangential resolution from the perspective of the reconstruction algorithms. As shown in the reconstructed images with MDAS algorithm (see Fig. 4(d)), the shape of the filament can be well retained for transducers with different apertures. Particularly, the distribution of multifilaments can still be clearly identified for transducers with a larger aperture size. Moreover, the initial pressure peaks reconstructed using the MDAS algorithm seem to be larger.

Figures 4(e) and 4(f) show the reconstructed images of MFs-01 with transducers of different apodization condition σ.

The reconstructed cross sectional images of multiple filaments preserve its shape for both algorithms when apodization parameter σ increases from 0.6 mm to 5.0 mm. As seen from the recovered initial pressure values, it seems that a larger σ is beneficial to improve the reconstruction effect. The larger apodization parameter σ means that the sensitivity of the detection points on the surface of the transducer is more homogeneous and therefore the reconstruction is better.

The structural similarity (SSIM) index is then used to quantitatively determine the performance of the reconstruction algorithms under PAT system parameters. The basic SSIM Index is a full-reference (FR) picture quality model defined between two luminance images of size $M \times N$, $I_1(i,j)$ and $I_2(i,j)$ as a multiplicative combination of three terms: luminance similarity $l(i,j)$, contrast similarity $c(i,j)$, and structure similarity $s(i,j)$[40]

$$Q(i,j) = l(i,j) \cdot c(i,j) \cdot s(i,j), \tag{11}$$

$$\mathrm{SSIM}(I_1, I_2) = \frac{1}{MN} \sum_{i=1}^{M} \sum_{j=1}^{N} Q(i,j). \tag{12}$$

The SSIM is a perceptual metric according to visible structures in the image. The higher the value of SSIM, the better the reconstruction.

Figure 5 presents the SSIM of the reconstructed images varies with PAT system parameters including the scanning radius D_r, central frequency f_c, aperture size L, and apodization condition σ. Both figures show that the SSIM increases as the target distance D_r increases, which means a larger scanning radius is beneficial to the increases of image quality.[27] As shown in Figs. 5(a) and 5(d), the center frequency affects the similarity of images obviously. The SSIM decreases as the center frequency of the transducer increases, which is possibly caused by the smaller size of a limited high-quality imaging region (HQIR) with a higher central frequency.[27] The apodization condition of transducer also affects the reconstructed images. As shown in Fig. 5(b), the SSIM declines as the apodization condition increases for CDAS algorithm. The conventional algorithm works best when σ is small, which has been also demonstrated in Ref. [25]. However, the apodization condition has less effect on the reconstructed images by the MDAS algorithm as shown in Fig. 5(e). This demonstrates the robustness of MDAS algorithm. The effect of aperture size of transducer on the result of reconstruction is shown in Figs. 5(c) and 5(f). For the CDAS algorithm, the regularity of SSIM variation with aperture size L is less pronounced. The SSIM for cross section reconstructed by MDAS tends to be lager for transducer with small-active-area. The smaller transducer size means wider angles to accept signals. However, the small-sized transducers have weaker sensitivity due to high thermal noise.[25] Overall, a PAT system with transducers of a lower central frequency (0.5 MHz–1.0 MHz) and a stronger apodization (< 1.0) working at a longer scanning radius (~ 3 mm) is recommended to be used in femtosecond laser multifilaments reconstruction.

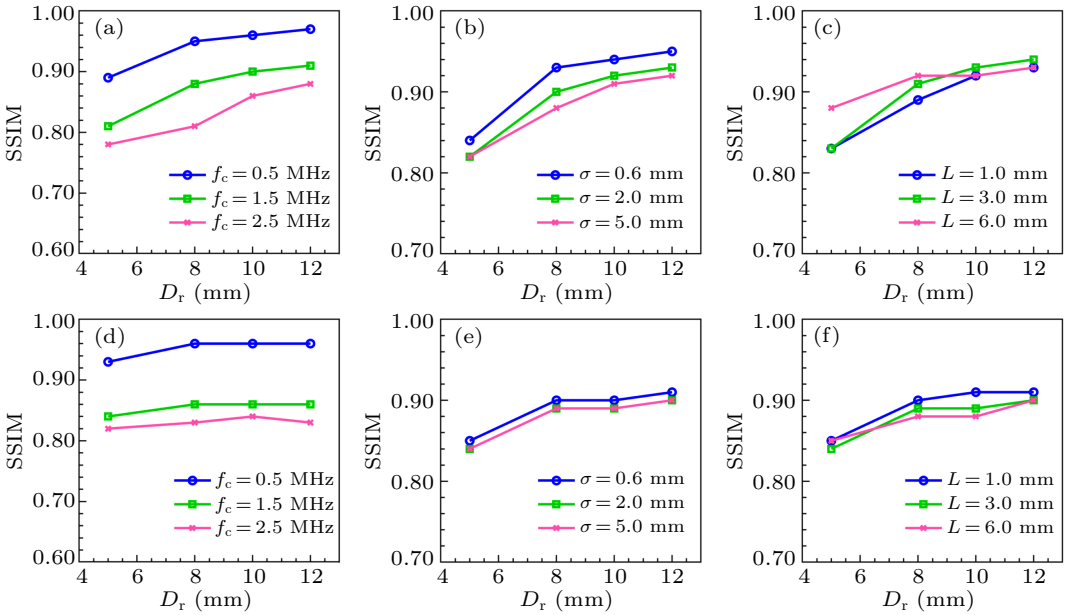


Fig. 5. Plots of SSIM as a function of distance of the source to the imaging center for flat transducer with different central frequency f_c [(a) and (d)], apodization condition σ [(b) and (e)], and aperture size L [(c) and (f)], where panels (a)–(c) are images reconstructed by CDAS algorithm and panels (d)–(f) are reconstructed by MDAS algorithm.

4. Conclusion and perspectives

We demonstrated that by using photoacoustic tomography (PAT), an emerging medical imaging technique, the transverse structures of femtosecond laser multifilaments can be properly reconstructed. A typical circular PAT system with finite-sized transducers is modelled to record the filament-

induced acoustic signals. Three types of measured cross-sectional images of multiple filaments (MFs) are used as input conditions for the forward propagation model. We find the frequency range of acoustic signal induced by MFs with maximum volumetric energy density $\sim$ 100 kJ/m^3 is below 2 MHz when propagated up to 5 mm away from the center through attenuation. By using the modified DAS (MDAS) algorithm modeling the transducer as a collection of small point detectors, the shape of "hot spots" in the filaments can still be appropriately reconstructed even with detectors of large aperture size and apodization. Thus, higher SNR reconstructed images are expected in practice. Such shape reconstruction is important for diagnosing the spatiotemporal dynamics of filamentation. A PAT system with transducers of a lower central frequency and a stronger apodization working at a longer scanning radius is recommended to be used in femtosecond laser multifilaments reconstruction. Additionally, since the reconstructed initial pressure distribution contains information of the energy deposition into the medium, which makes photoacoustic tomography a promising diagnostic method for laser-matter interactions. However, the back-projection (BP) based image reconstruction algorithm mainly obtains structural information instead of quantitative images. To obtain more quantitative imaging information on filaments, iterative image reconstructions or system matrix-based image reconstructions can be considered in the future.

Acknowledgements

Project supported by the National Natural Science Foundation of China (Grant No. 42105176) and the National University of Defense Technology Independent Research Project (Grant No. ZK21-40). The authors are grateful to Manojit Pramanik for his help with the photoacoustic tomography reconstruction algorithm.

References

[1] Couairon A and Mysyrowicz A 2007 *Phys. Rep.* **441** 47
[2] Durand M, Houard A, Prade B and Mysyrowicz A 2013 *Opt. Express* **21** 26836
[3] Huang X D, Zhang M, Deng L H, Pang S B, Liu K and Xu H L 2022 *Chin. Phys. B* **31** 097801
[4] Wolf J P 2018 *Rep. Prog. Phys.* **81** 026001
[5] Châteauneuf M, Payeur S, Dubois J and Kieffer J C 2008 *Appl. Phys. Lett.* **92** 091104
[6] Zhang Z, Lu X, Liang W X, Hao Z Q, Zhou M L, Wang Z H and Zhang J 2009 *Chin. Phys. B* **18** 1136
[7] Schimmel G, Produit T, Mongin D and Kasparian J 2018 *Optica* **5** 1338
[8] Shang B P, Zhang Z, Zhang N, Qi P F and Guo J W 2024 *IEEE Photon. Technol. Lett.* **36** 512
[9] Wei Y X, Wang T J, long J, Yin F K and Ding X Y 2023 *Opt. Express* **31** 6938
[10] Méchain G, Couairon A and André Y B 2004 *Appl. Phys. B* **79** 379
[11] Chen Y P, Théberge F, Kosareva O, Panov N, Kandidov V P and Chin S L 2007 *Opt. Lett.* **32** 3477
[12] Xu S Q, Sun X D, Zeng B, Chu W, Zhao J Y and Liu W W 2012 *Opt. Express* **20** 299
[13] Fedorov V Y and Tzortzakis S 2020 *Light: Science & Applications* **9** 186
[14] Wahlstrand J K, Jhajj N, Rosenthal E W, Zahedpour S and Milchberg A H M 2014 *Opt. Lett.* **39** 1290
[15] Arantchouk L, Honnorat B, Thouin E, Point G, Mysyrowicz A and Houard A 2016 *Appl. Phys. Lett.* **108** 173501
[16] Yu J, Mondelain D, Kasparian J and Salmon E 2003 *Appl. Opt.* **42** 1
[17] Point G, Thouin E, Mysyrowicz A and Houard A 2016 *Opt. Express* **24** 6271
[18] Rosenthal E W, Jhajj N, larkin I, Zahedpour S, Wahlstrand J K and Milchberg A H M 2016 *Opt. Lett.* **41** 3908
[19] Larkin I, Griff-McMahon J, Schweinsberg A, Goffin A, Valenzuela A and Milchberg H M 2020 *Opt. Lett.* **45** 2518
[20] Uryupina D S, Bychkov A S, Pushkarev D V, Mitina E V, Savel'ev A B, Kosareva O G, Panov N A and Karabutov A A 2016 *Laser Phys. Lett.* **13** 095401
[21] Kolesik M and Moloney J 2004 *Opt. Lett.* **29** 590
[22] Wang L V and Hu S 2012 *Science* **335** 1458
[23] Cheng Y H, Wahlstrand J K, Jhajj N and Milchberg H M 2013 *Opt. Express* **21** 4740
[24] Treeby B E, Jaros J, Rendell A P and Cox B T 2012 *Journal of the Acoustical Society of America* **131** 4324
[25] Warbal P, Pramanik M and Saha R K 2019 *J. Opt. Soc. Am. A* **36** 245
[26] Pramanik M 2014 *J. Opt. Soc. Am. A* **31** 621
[27] Luo X F, Jiang J S, Wu H L, Li M H and Wang B 2023 *Ultrasonics* **133** 107042
[28] Xu Y, Xu M H and Wang L H 2002 *IEEE Transactions on Medical Imaging* **21** 829
[29] Xu M H and Wang L H V 2005 *Phys. Rev. E* **71** 16706
[30] Omidi P, Yip L C M, Rascevska E, Diop M and Carson J J L 2022 *Photoacoustics* **28** 100404
[31] Treeby B E, Wise E S, Kuklis F, Jaros J and Cox B 2020 *Journal of the Acoustical Society of America* **148** 2288
[32] Potemkin F V, Mareev E I, Rumiantsev B V, Bychkov A S, Karabutov A A, Cherepetskaya E B and Makarov V A 2018 *J. Phys. Conf. Ser.* **1141** 012060
[33] Mejean G, Kasparian J, Yu J, Salmon E, Frey S, Wolf J P, Skupin S, Vincotte A, Nuter R, Champeaux S and Berge L 2005 *Phys. Rev. E* **72** 026611
[34] Liu W, Théberge F, Arevalo E, Gravel J F, Becker A and Chin S L 2005 *Opt. Lett.* **30** 2602
[35] Bychkov A S, Cherepetskaya E B, Karabutov A A and Makarov V A 2016 *Laser Phys. Lett.* **13** 085401
[36] Potemkin F V, Mareev E I, Rumiantsev B V, Bychkov A S and Karabutov A A 2018 *Laser Phys. Lett.* **15** 075403
[37] Shang B P, Zhang Z, Zhang N, Qi P F, Guo J W, Tao S S, Lin L and Liu W W 2024 *IEEE Photon. Technol. Lett.* **36** 512
[38] Shang B P, Qi P F, Guo J W, Zhang Z and Guo L J 2023 *Optics and laser technology* **157** 108636
[39] Rumiantsev B V, Mareev E I, Bychkov A S, Karabutov A A and Cherepetskaya E B 2021 *Appl. Phys. Lett.* **118** 011109
[40] Venkataramanan A K, Wu C Y, Bovik A C, Katsavounidis I and Shahid Z 2021 *IEEE Access* **9** 28872